Nanoscale

MINIREVIEW

View Article Online
View Journal | View Issue

Cite this: *Nanoscale*, 2025, **17**, 9895

Spin effects in metal halide perovskite semiconductors

Md Azimul Haque and Matthew C. Beard *

Metal halide perovskite semiconductors (MHSs) are emerging as potential candidates for opto-spintronic applications due to their strong spin–orbit coupling, favorable light emission characteristics and highly tunable structural symmetry. Compared to the significant advancements in the optoelectronic applications of MHSs, the exploration and control of spin-related phenomena remain in their early stages. In this minireview, we provide an overview of the various spin effects observed both in achiral and chiral MHSs, emphasizing their potential for controlling interconversion between spin, charge and light. We specifically highlight the spin selective properties of chiral MHSs through the chirality-induced spin selectivity (CISS) phenomena, which enable innovative functionalities in devices such as spin-valves, spin-polarized light-emitting diodes, and polarized photodetectors. Furthermore, we discuss the prospects of MHSs as spintronic semiconductors and their future development in terms of material design, device architecture and stability.

Received 10th January 2025,
Accepted 20th March 2025

DOI: 10.1039/d5nr00127g

rsc.li/nanoscale

1. Introduction

The tunable properties of metal halide semiconductors (MHSs) have been instrumental in extending their applications beyond photovoltaics including radiation detectors, light emission, thermoelectrics and catalysis.[1–5] Heavy inorganic atoms with large spin–orbit coupling (SOC) along with tunable molecular components that break inversion symmetry have enabled a large library of MHS compositions covering the UV to NIR regime along with a variety of structural dimensionalities. Replacing the A-site cation with a chiral ammonium cation ensures structural inversion symmetry breaking, resulting in a multitude of exotic properties generally absent in achiral MHSs.[6,7] In recent years, chiral metal halide semiconductors (CMHSs) have exhibited several unique spin functionalities such as circularly polarized photodetectors, spin-polarized light emitting diodes, chiral phonon-activated spin Seebeck (CPASS) effect, and chirality-induced spin selectivity (CISS).[8–11] These novel properties allow CMHSs to be used as a new tool to control spin in semiconductor systems and are thus a strong contender for next-generation spintronic applications.

Traditional inorganic semiconductors offer high charge carrier mobility but shorter spin lifetimes, while organic semiconductors exhibit longer spin lifetimes but limited mobility, resulting in shorter spin diffusion lengths. MHSs, with their tunable lattice symmetry, high spin polarization, and significant Rashba splitting at room temperature, provide a unique opportunity to overcome these limitations.[12] Similar to conventional semiconductors, spin injection in MHSs can be achieved by various mechanisms such as electrical, optical, and spin pumping.[13] Understanding the spin injection and transport process in MHSs is crucial for designing efficient spintronic device architectures and identifying optimal MHS compositions. Initial studies on MHS spintronics predominantly focused on 3D achiral halide perovskites based on methylammonium or cesium cations. However, the arrival of CMHSs has led to the emergence of a wide variety of chiral halide perovskites featuring diverse chiral A-site cations with intriguing spin-dependent properties. A major advantage of CMHSs is their ability to facilitate spin-selective charge transport based on the handedness of the lattice, as well as their demonstration of spin-polarized emission at room temperature. Such properties of CMHSs offer the potential for developing simpler, tunable spintronic structures capable of operating at room temperature without magnetic components.

In this minireview, we summarize the various aspects of spin phenomena in MHSs with a focus on their relevance to spintronic applications. A general overview of spintronic applications based on both achiral and chiral MHSs is provided, emphasizing the spin-selective characteristics of CMHSs. Emerging phenomena such as CISS and CPASS in CMHSs are discussed, highlighting their prospects and challenges. Furthermore, we explore the possible structure–property correlations among different spin parameters such as spin polarization, magnetoresistance and dissymmetry factors. Finally, we address the key questions and outline strategies for the future

---

*National Renewable Energy Laboratory, Golden, Colorado 80401, USA.
E-mail: matt.beard@nrel.gov*

development of MHSs as spintronic-type semiconductors. By integrating insights from material design, structural tunability, and spin transport mechanisms, this review aims to guide the realization of high-performance spintronic applications that leverage the unique capabilities of both achiral and chiral MHSs.

2. Metal halide perovskites: structure and functionality

Initial theoretical and experimental investigations into spin-related properties, such as spin splitting driven by Rashba or Dresselhaus type effects, were primarily based on 3D MHSs (Fig. 1a), such as methylammonium lead iodide ($MAPbI_3$) and methylammonium lead bromide ($MAPbBr_3$), motivated by the long charge carrier lifetime observed in MHS photovoltaic structures.[14–16] The 3D MHSs exhibited strong SOC and significant spin splitting encouraging their application for spintronics. Subsequently, large Rashba spin splitting was also observed in the commonly used 2D MHS, phenethylamine lead iodide, $(PEA)_2PbI_4$.[17] The Rashba splitting in layered 2D MHSs was found to be tunable as a function of layer number (Fig. 1b), offering an additional degree of control over spin coherence lifetimes.[18] Spin splitting in such centrosymmetric structures arises due to local asymmetry, cation rotation, phase transition, and phonon-assisted lattice deformation.[19–22]

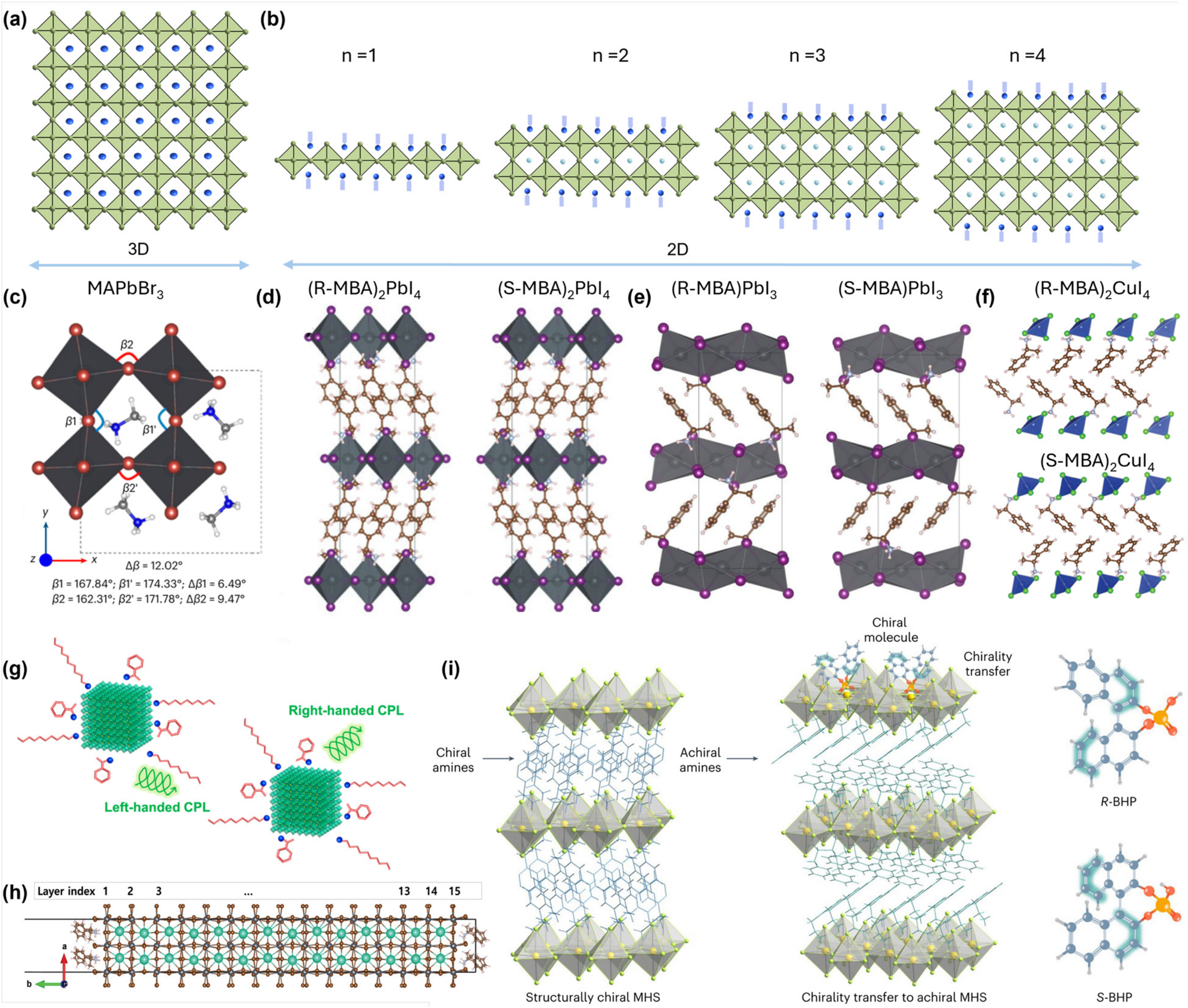

Fig. 1 Schematic structure of achiral (a) 3D and (b) 2D MHSs. (c) Chiral $MAPbBr_3$ structure. Reproduced from ref. 23 with permission from Nature Publishing Group, Copyright 2023. (d) Structures of $(R\text{-MBA})_2PbI_4$ and $(S\text{-MBA})_2PbI_4$. Reproduced from ref. 24 with permission from the Royal Society of Chemistry, Copyright 2017. (e) Structures of $(R\text{-MBA})PbI_3$ and $(S\text{-MBA})PbI_3$. Reproduced from ref. 8 with permission from Nature Publishing Group, Copyright 2019. (f) Structures of $(R\text{-MBA})_2CuCl_4$ and $(S\text{-MBA})_2CuCl_4$. Reproduced from ref. 25 with permission from American Chemical Society, Copyright 2021. (g) Post-synthetic ligand treatment of $FAPbBr_3$ nanocrystals. Reproduced from ref. 26 with permission from American Chemical Society, Copyright 2020. (h) DFT-derived 15-layer inorganic slab models of perovskite crystals with $[S\text{-MBA}]^+$ ligands. Reproduced from ref. 27 with permission from Wiley-VCH, Copyright 2022. (i) Structurally chiral MHSs and chirality transfer in achiral MHSs along with the molecular structure of *R*/*S*-BHP. Reproduced from ref. 28 with permission from Nature Publishing Group, Copyright 2024.

In recent years, there has been a surge in research on the spin transport properties of CMHSs motivated by the correlation between their structural chirality and spin selectivity. 3D CMHSs have been developed in the form of meta-structures and single crystals.[23,29,30] The addition of nucleation agents, such as micro- or nanoparticles, has been used to template the A-site cations into chiral patterns, resulting in chiral 3D MHS structures (Fig. 1c). Most CMHSs, however, adopt a 2D MHS structure featuring a chiral ammonium cation at the A-site. The incorporation of the chiral A-site cation breaks the structural symmetry of the MHS, generating left and right-handed chiral structures (Fig. 1d). There are also 1D (Fig. 1e) and 0D (Fig. 1f) variants; however, majority of the demonstrations of spin control and functionality are based on 2D CMHSs.[31] In a stricter sense, 1D and 0D structures are essentially hybrid metal halides rather than perovskites.[32] 3D CMHSs in the form of nanocrystals with chiral ligands on their surface represent a facile approach for achieving chiroptical properties.[26] Postsynthetic ligand exchange of MHS nanocrystals (Fig. 1g) with chiral ligands distorts the surface lattice (Fig. 1h) that penetrates a few unit cells leading to CMHS nanocrystals with left and right-circularly polarized emission. Interestingly, recent advancements have shown that CMHSs can also be synthesized using achiral building blocks.[28,33] This emerging strategy simplifies the synthetic chemistry and offers new possibilities. In achiral 2D MHSs, chirality can be remotely induced by introducing non-ammonium, non-A-site chiral molecules that do not directly integrate into the MHS structure but break the symmetry by distorting the inorganic sub-lattice (Fig. 1i). Such a strategy eliminates the need for mandatory chiral ammonium cations and expands the library of potential chiral inducers, offering a broad range of molecules with diverse sizes and properties for exploration.

3. Spin effects in MHSs

The presence of strong SOC in MHSs combined with their highly tunable structural symmetry offers a range of spin-dependent phenomena. These effects include pronounced spin textures, extended and controllable spin lifetimes, and circularly polarized light emission. Such properties position MHSs as promising candidates for next-generation spintronic applications. In this section, we provide a summary of the diverse spin-related effects observed in MHSs. We further explore the emerging field of CMHSs as novel platforms for controlling spin in a variety of heterostructures and their applications. The discussion is centered on traditional spintronic types of applications such as spin-valves that incorporate the CISS effect, where the selective transport and control of spin-polarized carriers play a critical role. A comparative analysis of key performance parameters, including spin polarization efficiency, circular dichroism (CD) dissymmetry factor, and magnetoresistance, is conducted to determine if any correlations exist. The integration of these unique properties into spin architecture offers new opportunities for developing highly efficient, energy-saving electronic devices for quantum information processing, communications, displays, memory storage, and opto-spintronics.

3.1. Spin splitting

The majority of the MHS compositions, which predominantly consist of heavy atoms such as Pb and I, exhibit significant spin splitting due to the spin–orbit coupling (SOC) effects. In a non-centrosymmetric crystal environment, the combination of SOC and broken inversion symmetry culminates in the crystal momentum spin splitting of the frontier electronic bands through the Rashba–Dresselhaus effect. The SOC perturbates the Hamiltonian of the system, which is proportional to $(\nabla V \times p)\cdot\sigma$, where V is the crystal potential, p is the momentum operator, and σ is the spin operator, giving rise to specific spin textures in the conduction and valence bands.[19] Local asymmetry in both the potential and the wave function in the core regions of heavy nuclei governs the spin splitting.[34] The Rashba–Dresselhaus effects are particularly of great importance as they enable spin-orbitronic functionalities including generating, detecting, and modulating spin currents.[14,35–39] Breaking of the inversion symmetry in MHSs is key to observing spin splitting, and a number of factors affect the symmetry breaking, including phase transitions, cation rotation, asymmetric hydrogen bonding, and surface termination. Significant spin splitting in MHSs has already been demonstrated experimentally by several different techniques, among which the Rashba splitting in the single crystal $MAPbBr_3$ surface measured by angle-resolved photoemission spectroscopy (ARPES) serves as a seminal example.[15] Fig. 2a–e depict the spin splitting phenomena for broken inversion symmetry and band splitting of $MAPbBr_3$. Under SOC, a doubly spin-degenerate band splits and shifts in the k space relative to each other. $MAPbBr_3$ shows Rashba splitting in both orthorhombic and cubic phases with the Rashba parameter (α) being 7 eVÅ and 11 eVÅ, respectively, which are among the highest values. Rashba effects have also been observed in other 3D MHSs such as $MAPbI_3$ and $MAPbI_xBr_{3-x}$ and it was attributed to the presence of ionic impurities and halide alloying, respectively, leading to inversion symmetry breaking.[35] Such spin-splitting phenomena in MHSs open pathways for exploring a variety of exotic spin-dependent processes such as the spin-Hall effect, gate-controlled spin precession, spin and photo galvanic effects, and chiroptical effects.[19]

Like their 3D counterparts, 2D MHSs also exhibit strong Rashba effects, primarily due to inverse symmetry breaking within their layered structures. The octahedral distortions along with the alternating organic–inorganic components in 2D MHSs offer additional tunability over symmetry breaking.[35,40] This tunability is particularly relevant in the context of chirality, as most CMHSs are structurally 2D. In CMHSs, the chiral A-site cation induces symmetry breaking by distorting the metal–halide (M–X) octahedra. In contrast to centrosymmetric MHSs, non-centrosymmetric MHSs exhibit bond angle disparities ($\Delta\beta$) in the M–X–M bonds, leading to symmetry breaking (Fig. 2f). The in-plane octahedral tilting

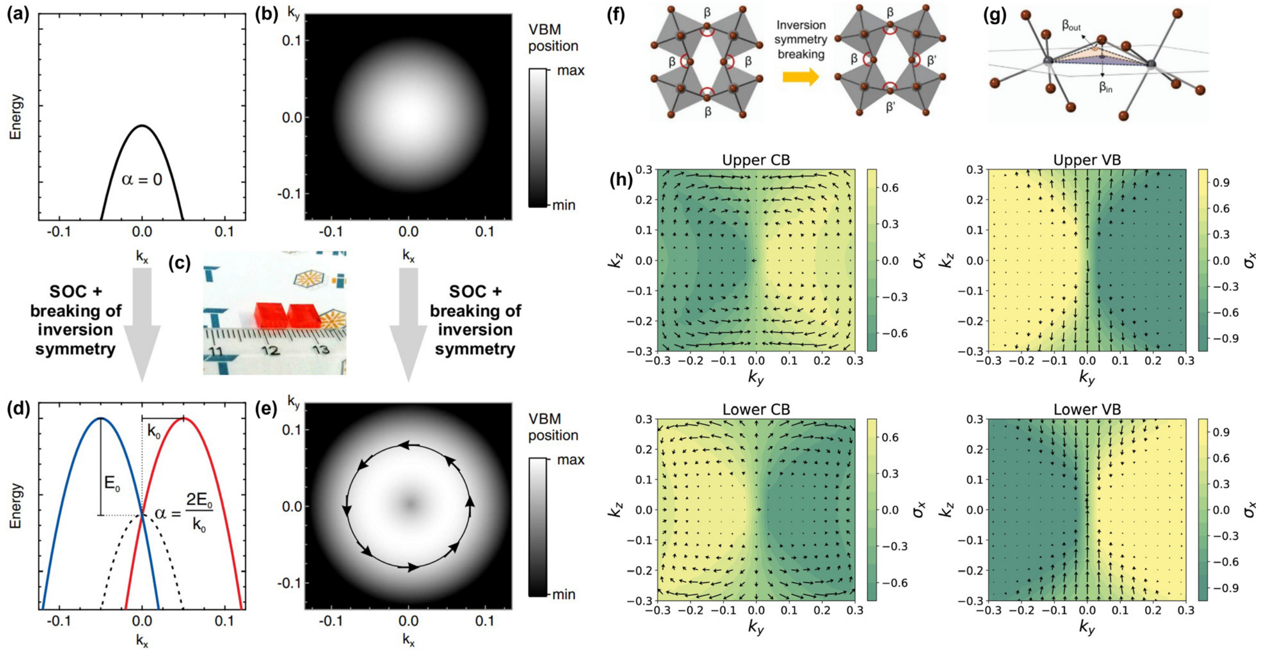

Fig. 2 (a) and (b) SOC and Rashba effects on VB dispersion. Without SOC, a doubly spin-degenerate band with a single maximum is expected. (c) Photograph of the single crystals. (d) and (e) In the presence of SOC and inversion-symmetry breaking fields, two spin-split bands are observed where the strength of the SOC is quantified using the Rashba parameter α. (e) Orientation of the in-plane component of the spin depicted by the arrows. Reproduced from ref. 15 with permission from APS, Copyright 2016. (f) Schematic showing symmetric (one bond angle, β) and asymmetric tilting (two bond angles, β and β') of octahedra where asymmetric tilting breaks the inversion symmetry. (g) In-plane (β_{in}) and out-of-plane (β_{out}) projections for β. (h) Spin polarization of CB and VB subbands projected onto the reciprocal 2D plane perpendicular to the stacking direction for the CMHS: [*S*-4-NO$_2$-MBA]$_2$PbBr$_4$·H$_2$O. The arrows and color scheme represent the in-plane components and the magnitude of the out-of-plane component, respectively. Reproduced from ref. 41 with permission from Nature Publishing Group, Copyright 2021.

asymmetry ($\Delta\beta_{in}$) correlates with the degree of spin splitting (Fig. 2g). Higher $\Delta\beta_{in}$ results in an inversion asymmetry within the inorganic layers (M–X), offering an indication of spin splitting.[41] A comprehensive library of CMHS compositions linking structural distortions with spin-splitting properties can serve as a valuable resource for the rapid identification of potential candidates for spintronic applications. Another effective method for estimating spin splitting involves density functional theory (DFT) calculations. Spin polarization calculations that reveal opposite polarizations in split bands indicate a Dresselhaus-type spin texture, arising from bulk inversion asymmetry (Fig. 2h). Giant spin splitting exceeding 400 meV, along with persistent spin textures computed *via* DFT, has been observed in achiral 3D and 2D MHSs, making them attractive for applications such as spin field effect transistors and valley spin-valves.[19,42] While DFT has become a standard tool for predicting spin splitting and spin textures, it is crucial to correlate these theoretical insights with experimental observations, particularly at room temperature. Bridging the gap between computational predictions and experimental validation is essential for advancing the design and application of MHS-based spintronic devices.

3.2. Spin lifetime

Spin lifetime is a critical parameter for efficient spin transport and plays a vital role in the performance of spintronic devices. Several factors influence spin lifetime, including material defects, spin–phonon interactions, crystallinity, and measurement temperature and techniques. The tunable composition and structural symmetry of MHSs offer the possibility of tuning the spin lifetimes in this class of semiconductors. The most common method for measuring the spin lifetime is circularly polarized pump–probe (CPPP) spectroscopy (Fig. 3a). In this method, a circularly polarized pump pulse is used to spin-orient carriers, while a circularly polarized probe pulse is employed to monitor the spin-relaxation dynamics.[43] According to the optical selection rules (Fig. 3b) for free carriers in MHSs, left or right-circularly polarized light (LCP/RCP) excites electrons from the valence band (VB) with $m_J = -1/2$ (1/2) state to the conduction band (CB) $m_J = 1/2$ ($-1/2$) state while conserving angular momentum (*i.e.* $\Delta m_j = \pm 1$). Although the CPPP technique is highly relevant for spin devices relying on photoexcitation, for devices involving electrical spin injection, spin lifetime measurements using the electrical Hanle effect are more useful for elucidating the spin-physics. To measure the spin lifetime using the Hanle effect for a spin-valve comprising two ferromagnet (FM) electrodes separated by an MHS layer, an out-of-plane external magnetic field, B_z, is applied when the magnetization directions of the two FM electrodes are aligned in the parallel or antiparallel configuration. The injected spin from one FM electrode will precess due to the

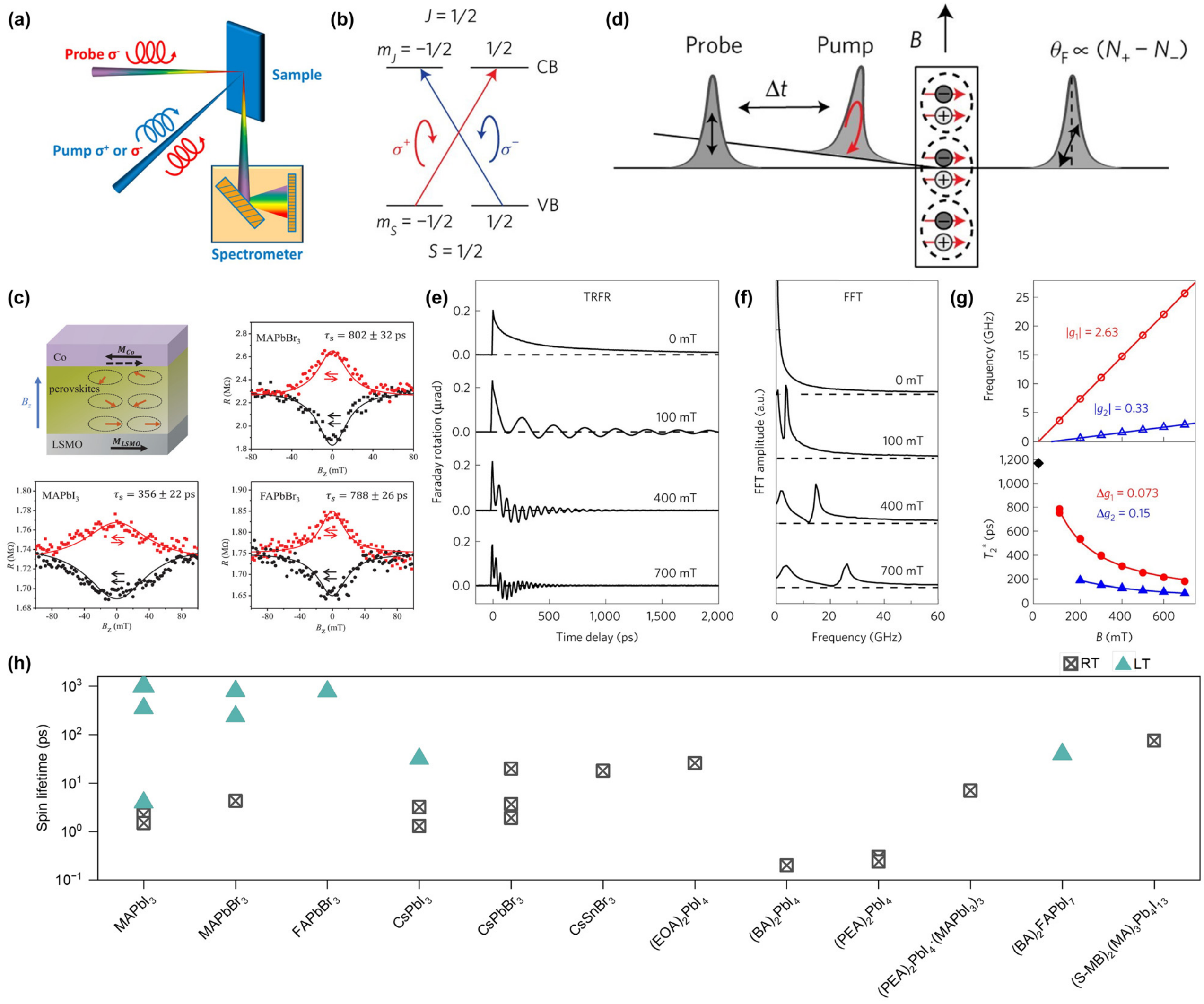

Fig. 3 (a) Schematic of the circularly polarized pump–probe technique for spin-relaxation dynamics measurement. Reproduced from ref. 43 with permission from American Chemical Society, Copyright 2024. (b) Spin-dependent optical transitions for $CH_3NH_3PbI_3$ near the bandgap. Reproduced from ref. 16 with permission from Nature Publishing Group, Copyright 2017. (c) Schematic showing the Hanle effect in a MHS spin-valve device. The quenching response of $GMR_{max}(B_z)$ due to the spin precession around B_z measured for $MAPbBr_3$, $MAPbI_3$, and $FAPbBr_3$ based spin-valves at 10 K. Reproduced from ref. 44 with permission from Wiley-VCH, Copyright 2019. (d) Schematic of the time-resolved Faraday rotation measurement in the Voigt geometry. (e) Time traces of TRFR. (f) Fast Fourier transform (FFT) of the TRFR curves. (g). Oscillation frequencies *versus* the magnetic field for the two components (top) and the T2 transverse magnetic field *B* (bottom). Reproduced from ref. 16 with permission from Nature Publishing Group, Copyright 2017. (h) Spin lifetime of some representative MHSs at room and low temperatures measured by various techniques such as CPPP, Hanle, and TRFR.[16,18,43–45,49–58] RT: room-temperature, LT: low-temperature.

transverse magnetic field while diffusing in the MHS interlayer toward the opposite FM electrode, causing the resulting magnetoresistance to increase or decrease depending on whether the two FMs are parallel or antiparallel.[44] The Hanle effect-based spin lifetimes for $MAPbBr_3$, $FAPbBr_3$, and $MAPbI_3$ have reported values of 802, 788, and 356 ps at 10 K, respectively (Fig. 3c). Similar spin lifetime values for MA and FA-based MHSs indicate a negligible effect of the A-site cation, while a shorter spin lifetime in the case of $MAPbI_3$ compared to $MAPbBr_3$ suggests the critical role of halogens as well as an inorganic sublattice in determining the spin transport behavior. It should be noted that spin lifetime can also be assessed using the optical Hanle effect, where the external magnetic field is applied perpendicular to the photoluminescence light propagation direction or spin orientation leading to spin precession and a reduction in the circular polarization of the emitted PL.[45]

A variation of the CPPP technique is time-resolved Faraday rotation (TRFR). Here, a circularly polarized pump pulse optically orients spin-polarized carriers along the beam axis and the rotation of a linearly polarized probe beam is measured in response as a function of time delay between the circularly polarized pump and the probe pulse (Fig. 3d). Typically a transverse magnetic field is applied while exciting the material with the circularly polarized light, enabling the same Hanle effect mentioned above from the optically oriented carriers.[16] Classically, the photogenerated spins precess around the external field leading to periodic oscillations in the Faraday rotation whose frequency is proportional to the *g*-factor. Quantum mechanically, there is an oscillating superposition of quantum states resulting in oscillations in the Faraday rotation over time. Fig. 3f–h depict the TRFR response of $CH_3NH_3PbCl_xI_{3-x}$ under varying magnetic field strengths. Under zero magnetic field, a typical bi-exponential decay is observed, which transitions to an oscillatory response under an applied magnetic field, a characteristic of quantum beating due to spin precession (Fig. 3e). The zero field spin lifetime at 4 K exceeds 1 ns, which is unusually high given the strong SOC in MHSs. Fast Fourier transform (FFT) spectra of the TRFR signals reveal two distinct oscillation frequencies (Fig. 3f). These frequencies are proportional to the applied magnetic field (Fig. 3g) and correspond to *g*-factors for electrons (−0.33) and holes (2.63). Spin–orbit interactions cause the *g*-factor to deviate from its vacuum value of 2.[46] Understanding and controlling the *g*-factor (by doping) under electric and magnetic fields is an important avenue for tunable spintronic applications.[47] While low-temperature spin lifetimes measured by various techniques are typically high, room-temperature spin lifetimes are almost two orders of magnitude lower, which is crucial for the development of room-temperature spintronics (Fig. 3h). Pure 2D MHSs generally exhibit short spin lifetimes, with a notable exception where a μs lifetime has been observed.[48] In contrast, quasi-2D MHSs exhibit spin lifetimes comparable to those of 3D MHSs. Strategies to enhance room-temperature spin lifetime in MHSs need to focus on optimizing SOC, spin–phonon coupling, and sample quality.

3.3. Harnessing spin effects

Compared to the spin-physics in conventional semiconductors, the understanding, control, and application of spin functions in MHSs are still in their early stages. Nevertheless, several architectures based on traditional spintronics have been developed to both investigate the fundamental spin properties and facilitate practical applications. The two most commonly studied spin properties include spin lifetime (discussed previously) and magnetoresistance in the form of a spin-valve. In achiral MHSs, high spin lifetimes and diffusion lengths at low temperatures contribute to the development of spin-valves with decent magnetoresistance (MR). A typical spin-valve consists of two FM electrodes with an MHS layer sandwiched between them (Fig. 4a). A spin-valve under an applied magnetic field exhibits low and high resistance states depending on whether the magnetizations of the FM electrodes are aligned in parallel or antiparallel, resulting in a giant magnetoresistance (GMR) response.[45] Another notable demonstration of spin phenomena in achiral MHSs is the spin-polarized light-emitting diode (spin-LED). In a traditional spin-LED, spin injection occurs through an FM electrode, leading to circularly polarized electroluminescence (CPEL) from the light-emitter layer. It is important to note that for achiral MHSs, an FM electrode and an applied magnetic field are required to observe CPEL. For $MAPbBr_3$, 3.1% degree of polarization (circularly polarized emission) and 0.8% CPEL have been demonstrated at 10 K.[45] While these examples of achiral 3D MHSs serve as proof-of-concept spintronic devices, the major limitation lies in their operation at cryogenic temperatures. For widespread practical applications, room temperature spin effects are critical.

CMHSs offer several advantages over their achiral counterparts in harnessing spin, including the potential for room temperature operation, large spin polarization, and a reduced number of magnetic layers. CMHSs exhibit natural spin selectivity based on the chirality of their lattice. CMHSs manifest several intriguing spin phenomena such as chirality-induced spin selectivity (CISS), the circular photogalvanic effect (CPGE), circularly polarized light (CPL) emission, and the chiral phonon-activated spin Seebeck (CPASS) effect. Among these, CISS plays a central role in realizing room-temperature CMHS spin-LEDs and spin-valves. In essence, CISS refers to the colinear spin-polarization of charge carriers as they pass through a chiral medium.[59,60] The first demonstration of CISS in CMHSs was in a spin-valve where the opposite handedness of the CMHS structure produced opposite MR responses, indicating that spin-polarized carriers experience CISS as they transverse the CMHS.[11] Unlike traditional spin-valves, CISS-based spin-valves consist of only one FM electrode, as the low and high resistance states are determined by the chirality of the CMHS layer and the FM polarization, simplifying the spin-valve architecture. A significant breakthrough in CISS was the realization of a room-temperature spin-LED by employing a spin-selective CMHS layer in conjunction with an achiral emissive layer. Spin-polarized carriers injected into the achiral emissive layer recombine selectively, emitting CPEL (Fig. 4b). The spin selectivity of CMHSs has also been explored in concert with traditional III–V semiconductors, leading to room-temperature spin accumulation in spin-LEDs with a CPEL polarization of 15%.[61] Additionally, CMHSs can be employed for CPL detection. When illuminated with LCP or RCP light, the CPL detector generates unequal photocurrents, thereby distinguishing the light polarization (Fig. 4c). As CMHSs have different absorptions for LCP and RCP light, CPL might lead to dissimilar photogenerated carrier densities. Consequently, these photogenerated carriers may experience different drifts during transport, a manifestation of CISS.[62] CPL detectors are essential components in technologies relevant to drug screening and quantum optics.[8] Beyond 2D CMHSs, 1D and 0D hybrid metal halides have also been explored as CPL detectors. In general, 1D hybrid metal halides exhibit high g_{CD} values that translate into a high degree of CPL detection.[63] CPL detectors are one of the simplest devices for harnessing the spin-selective properties of CMHSs.

The concept of CPL detectors has been extended to synaptic memristors (Fig. 4d), enabling the creation of unclonable cryptographic keys using polarized light.[64] By combining MHS chirality with neuromorphic functionality, it becomes possible to realize all-optical memory devices that operate with low

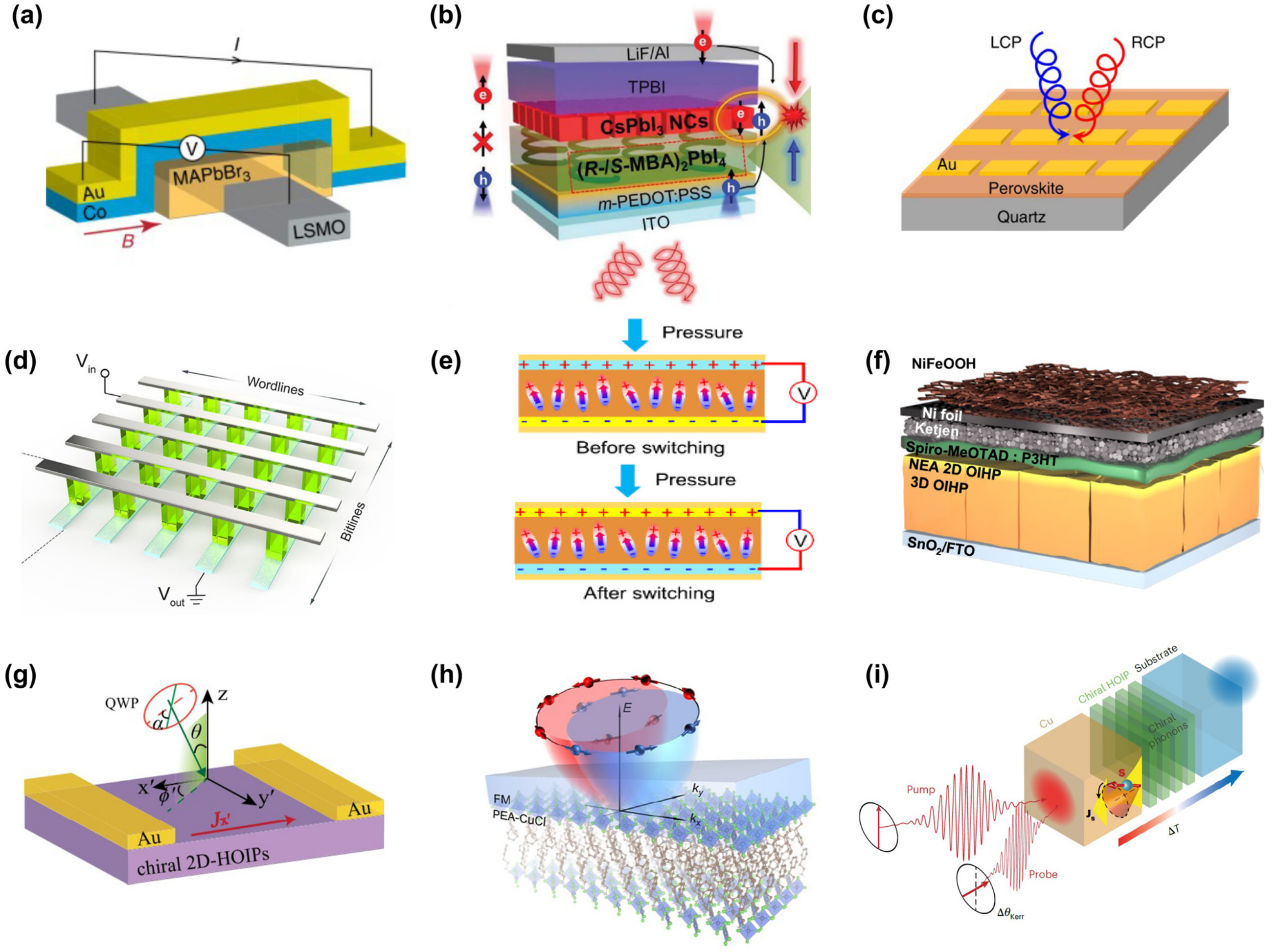

Fig. 4 (a) Schematic of an LSMO/MAPbBr$_3$/Co spin-valve. Reproduced from ref. 45 with permission from Nature Publishing Group, Copyright 2019. (b) Spin-polarized charge injection and CPEL emission in spin-LEDs. Reproduced from ref. 9 with permission from the American Association for the Advancement of Science, Copyright 2021. (c) Schematic device architecture of a circularly polarized photodetector. Reproduced from ref. 8 with permission from Nature Publishing Group, Copyright 2019. (d) Chiroptical synaptic memristor array. Reproduced from ref. 64 with permission from American Chemical Society, Copyright 2024. (e) CMHS-based piezoelectric device. Reproduced from ref. 65 with permission from Wiley-VCH, Copyright 2024. (f) Schematic illustration of a 3D-MHS/2D-CMHS photoanode. Reproduced from ref. 66 with permission from Nature Publishing Group, Copyright 2024. (g) Experimental setup for measuring the photogalvanic current in CMHSs. Reproduced from ref. 62 with permission from American Chemical Society, Copyright 2021. (h) Spin-momentum locking due to IRE of (PEA)$_2$CuCl$_4$/FM. Reproduced from ref. 67 with permission from American Chemical Society, Copyright 2024. (i) Measurement geometry of the CPASS effect in Cu/CMHS heterostructures. Reproduced from ref. 10 with permission from Nature Publishing Group, Copyright 2023.

power consumption. Furthermore, CMHSs with added piezoelectricity functionality (Fig. 4e) have been demonstrated for ultrasound detection under water.[65,68] The relatively low mechanical strength of CMHSs results in significant piezoelectric strain, which is advantageous for mechanoelectrical energy harvesting. An emerging application of CISS is in asymmetric catalysis, where spin selectivity is harnessed to enhance product formation or suppress byproducts compared to traditional achiral catalysts.[69] CISS-based catalysis has also been explored in the context of CMHSs, with 3D MHSs serving as light absorbers and 2D CMHSs acting as spin polarizers (Fig. 4f), resulting in a high spin polarization of 75% for the 2D/3D photoelectrode.[66]

In addition to the aforementioned applications, several other architectures have been investigated to study fundamental spin properties such as CPGE, spin generation, and the spin Seebeck effect. CPGE allows for control over the polarity and magnitude of photocurrents utilizing the chirality of elliptically polarized light in gyrotropic media. This effect arises from the asymmetric distribution of the excited charge carriers' momentum when exposed to LCP or RCP light, governed by spin–orbit coupling and angular momentum selection rules.[70] While for CISS, the transport measurement is typically out of plane (co-linear with the current direction), CPGE is measured in an in-plane geometry (Fig. 4g). CMHSs exhibit CPGE when illuminated with polarized light owing to the Rashba splitting in the electronic bands.[62] If the degree of CPGE can be correlated with the amount of Rashba splitting in CMHSs, a quantifiable parameter will emerge relevant for harnessing spin splitting. Another mechanism to exploit spin splitting is the interfacial Rashba effect (IRE). Forming heterostructures naturally breaks the inversion symmetry at the interface, thereby expanding the material choice. In this context, heterostructures of Pb-free 2D MHS $(PEA)_2CuCl_4$ with FM have been shown to act as room-temperature spin generators by the IRE mechanism (Fig. 4h). IRE in this architecture originates from strong interfacial orbital hybridization between the MHS and FM, measured using the spin-torque ferromagnetic resonance (ST-FMR) technique.[67]

Similar to CISS, which primarily relates to the spin polarization of charge carriers, the CPASS effect pertains to chiral phonons and their influence on spin transport. In CPASS, chiral phonons with angular momentum transmit spin information under a thermal gradient even in the absence of carriers, with the resulting spin currents depending on the handedness of the chiral medium (Fig. 4i). The CPASS effect in CMHSs transfers the angular momentum of chiral phonons to carriers in a proximal normal metal (copper) measured using the induced Kerr rotation.[10] A major advantage of CPASS is its applicability to low-conductivity chiral semiconductors and even insulators, without the need for magnetic contacts. CPASS demonstrates potential for spin caloritronic applications, as well as providing insights into the role of chiral phonons in spin generation and transport in chiral semiconductors.

3.4. Magnetoresistance

Magnetic junctions and their behavior under applied magnetic fields play a crucial role in various spintronic architectures. MHSs exhibit significant magneto-photocurrent, magneto-electroluminescence and magneto-photoluminescence responses, even in the absence of magnetic electrodes, due to magnetic field-induced spin mixing.[71] In the case of MHSs, magnetic junctions can be exploited for polarized PL emission, spin-LEDs, and spin-valves.[45,72] Here, we focus on spin-valves as they provide critical information on spin polarization, spin transport, and magnetoresistance. Spin-valves also underpin practical applications such as magnetic sensors, hard disk read heads, and magnetic random-access memories (MRAM). Initial works on MHS spin-valves focused on 3D achiral MHSs, employing two FM electrodes (Fig. 5a). Spin-valves based on $MAPbBr_3$, $MAPbI_3$, and $FAPbBr_3$ exhibit low-temperature GMR in the range of 4–25% (Fig. 5b–d), consistent with their spin lifetime trend.[44] Under an in-plane applied magnetic field, the magnetization orientations of the two FM electrodes (*e.g.*, LSMO and Co) align either parallel or antiparallel, resulting in low and high resistance states, respectively. Leveraging the photoactive properties of MHSs, a high MR of 97% has also been demonstrated in $MAPbI_3$ spin-valves.[73]

The advent of CMHSs has introduced new possibilities for spin-selective transport in spin-valves *via* the CISS effect. The handedness of CMHSs is typically determined through CD spectroscopy which measures the differential absorption of left- and right-handed CPL. Positive and negative CD values are observed for CMHSs with opposite chirality (Fig. 5e). This opposite chirality manifests as preferential spin-polarized carrier transport in spin-valves. Unlike traditional or achiral MHS-based spin-valves, CISS spin-valves are technically half spin-valves as they require only one FM electrode. In an archetypal CISS spin-valve, the CMHS is sandwiched between an FM and a non-magnetic electrode and the resistance is measured as a function of applied magnetic field. Depending on the chirality, carriers experience opposite spin polarization when passing through the CMHS layer, resulting in an opposite MR response (Fig. 5f and g). The MR response follows the hysteresis loop of the FM electrode. In the case of achiral 2D MHSs such as $(PEA)_2PbI_4$, the MR response is not consistent with the FM electrode and exhibits anisotropic MR and thus does not demonstrate CISS (Fig. 5h).

Reports on CMHS spin-valves remain limited, and the MR values are still relatively low. However, these studies provide valuable insights into spin transport and its dependence on various factors. Notably, while the spin polarization (SP) of CMHSs, as measured by magnetic-atomic force microscopy (m-AFM), is typically high, this does not always translate into correspondingly high MR in spin-valves. In addition, the dependence of MR values on the degree of chirality is not yet well understood. The circular dichroism dissymmetry factor (g_{CD}), which accounts for CMHS thickness, serves as a useful parameter for comparing the degree of chirality among different CMHS compositions. A comparative analysis of MR values against their g_{CD} and SP values reveals no clear trend (Fig. 5i–k). For instance, $(R/S\text{-MBA})_2PbI_4$ exhibits low g_{CD} but higher SP and modest MR. In contrast, the mixed CMHS $(R/S\text{-MBA})_2PbI_2Br_2$ shows lower g_{CD} and SP but higher MR. $(R/S\text{-MBA})_2SnI_4$ has very high SP but spin-valves of this composition have not been reported. While these comparisons currently lack a discernible pattern, it is plausible that a trend may emerge as more studies and data become available.

4. Future outlook

This minireview highlights the emerging spin properties and applications of achiral and chiral MHSs. The strong SOC intrinsic to MHSs results in significant spin splitting and long low-temperature spin lifetimes, establishing MHSs as promising candidates for spin-based applications and fundamental investigations. In particular, chiral MHSs exhibit unique spin functionalities that further broaden their potential as versatile semiconductors. Future developments are expected to focus on stabilizing and optimizing MHS compositions, understanding structure–property correlations, and designing innovative architectures and heterostructures aimed at harnessing their spintronic potential.

Current state-of-the-art spintronic properties or applications primarily rely on pristine MHS compositions or compositions with mixed A-site and mixed halides. While doping MHSs has been difficult due to their self-compensating nature, significant progress has been made in incorporating foreign atoms, forming alloys and developing composites, leading to

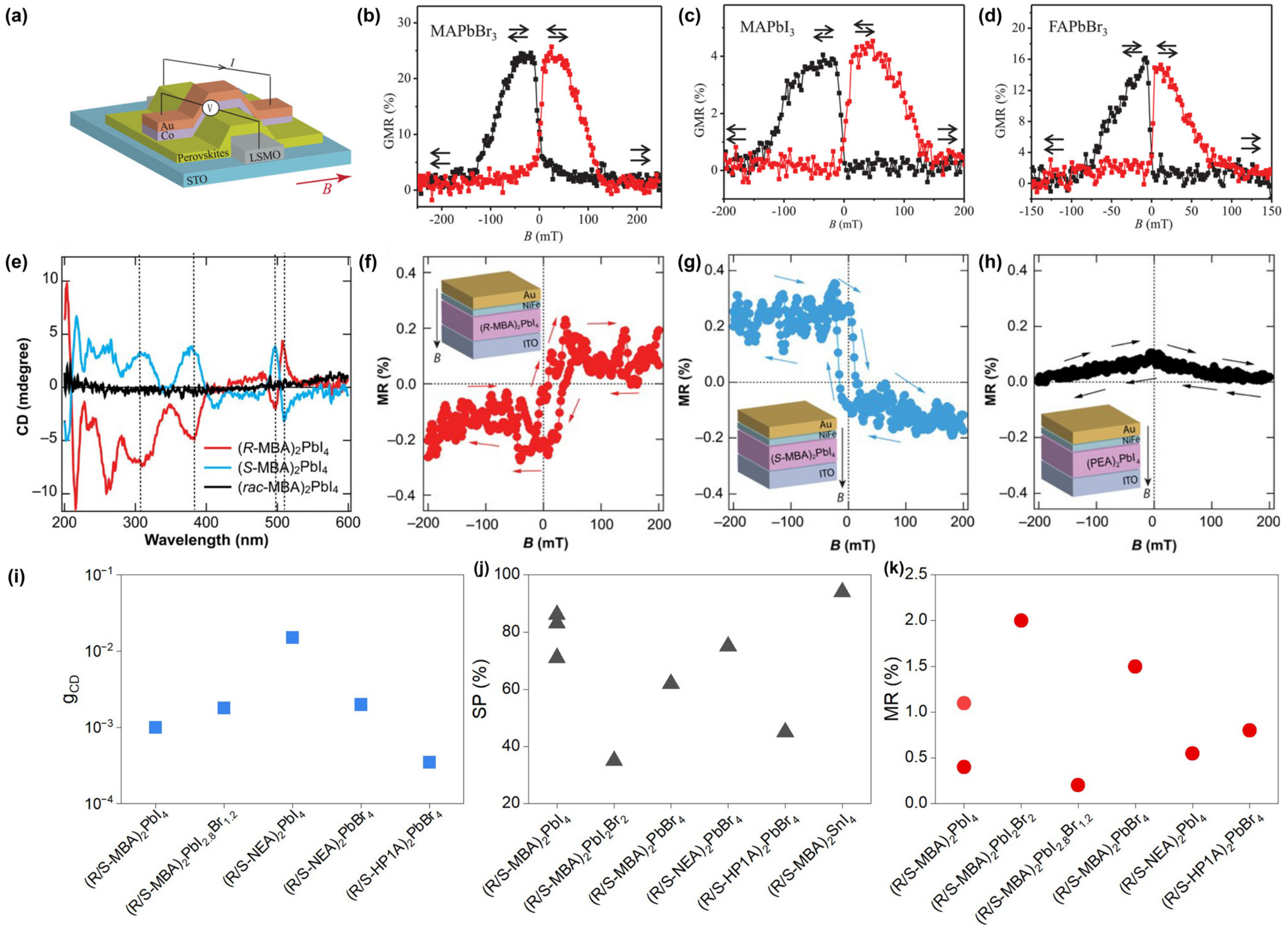

Fig. 5 (a) Achiral MHS spin-valve under an in-plane external magnetic field. GMR response of spin-valves based on (b) $MAPbBr_3$, (c) $MAPbI_3$, and (d) $FAPbBr_3$. Reproduced from ref. 44 with permission from Wiley-VCH, Copyright 2019. (e) CD spectra of $(R\text{-MBA})_2PbI_4$ and $(S\text{-MBA})_2PbI_4$ showing opposite signs. MR responses of spin-valves for (f) $(R\text{-MBA})_2PbI_4$, (g) $(S\text{-MBA})_2PbI_4$, and (h) $(PEA)_2PbI_4$. Reproduced from ref. 11 with permission from the American Association for the Advancement of Science, Copyright 2019. (i–k) g_{CD}, spin polarization (SP), and MR of some representative CMHSs.[11,66,74–78] Values in (i–k) are selected for either *R* or *S* handedness, whichever is higher.

improved electrical properties and even the induction of ferromagnetism.[47,79–82] These doped variants, both in achiral and chiral forms, can offer additional tunability to the MHS spin properties. The spin lifetimes of CMHSs remain low compared to their 3D achiral counterparts. Quasi-2D MHSs have shown promise with improved spin lifetimes compared to pure 2D systems. We believe the recent developments in simplifying the synthetic chemistry of CMHSs can greatly accelerate the material screening process and the relevant properties.[28] Compositional design considering spin manipulation needs to be developed to harness the full potential of CMHSs.

In terms of structure–property correlations, there is a significant gap in the literature associating the spin properties with the MHS composition. In 3D MHSs, it has been observed that while the A-site cation does not significantly impact the spin lifetimes, the inorganic framework plays a pivotal role.[44] In the case of 2D MHSs, structures with higher layer numbers demonstrate enhanced spin lifetimes.[18] However, spin lifetime measurements vary based on the techniques used and the operating temperatures, emphasizing the need to select appropriate methodologies (optical or electrical) based on the underlying device physics. Emerging insights into the effects of structural distortions on spin splitting in 2D MHSs underscore the importance of material symmetry in determining spin effects.[41] Since spin splitting is an important parameter for spintronic applications and has strong dependence on the MHS structure, a correlation between the MHS symmetry and the resulting spin splitting can serve as a key factor for accelerated materials screening. Developing a comprehensive database of MHS compositions and their spin properties is essential for fast-tracking material screening for specific spintronic applications.

The most prominent spintronic applications of MHSs are spin-LEDs and spin-valves. Spin-LEDs based on the CMHS spin-filtering layer with either achiral MHS emitter layers or traditional (III–V) emitter layers have been demonstrated.[9,61] However, the long-term stability of spin-LEDs warrants further attention for their development as a viable technology. Stable

MHS compositions, interface engineering, and efficient spin-polarized carrier injections are critical fronts for realizing high-performance spin-LEDs. CMHS compositions with enhanced structural and electrical stability can contribute to the operational stability of spin-LEDs. To this end, core–shell structures, quasi 2D CMHSs, and 2D/3D heterostructures are promising candidates.[83–85] Electrical stability under high bias conditions must also be investigated to understand the role of ion migration in device performance. Furthermore, innovative functionalities, such as controlling light polarization *via* electrical pulses, could pave the way for next-generation MHS-based spin-LEDs.[86] The low electrical conductivity of pure 2D MHSs poses a bottleneck for spintronic devices, necessitating strategies to enhance charge transport for efficient spin-polarized carrier collection. Despite the high spin polarization observed in the case of CMHSs, the MR is still very low. This brings into question whether the spin polarization measurements by m-AFM are overestimated. In addition, the optimization of CMHS spin-valve architecture has not received enough attention. Spin-valves are important for understanding several key spin properties such as magnetic field effects, spin injection and transport efficacy, and spin polarization. Special attention should be paid to the quality of the CMHS layer and its interface with the FM electrode in spin-valves to ensure high MR. More careful measurement and analysis is required for MHSs to understand the spin properties and their development as spintronic semiconductors. The development of CMHSs with enhanced spin lifetimes and stability, coupled with advanced characterization techniques, will be crucial for their integration into novel spintronic technologies such as neuromorphic computing, quantum information processing, and spin-caloritronics.

Data availability

No primary research results, software or code have been included and no new data were generated or analysed as part of this review.

Conflicts of interest

There are no conflicts to declare.

Acknowledgements

This work was supported within the Center for Hybrid Organic Inorganic Semiconductors for Energy (CHOISE), an Energy Frontier Research Center funded by the Office of Basic Energy Sciences, Office of Science within the U.S. Department of Energy. This work was authored in part by the National Renewable Energy Laboratory, operated by the Alliance for Sustainable Energy, LLC, for the U.S. Department of Energy (DOE) under Contract No. DE-AC36-08GO28308. The views expressed in the article do not necessarily represent the views of the DOE or the U.S. Government.

References

1 C. Fei, N. Li, M. Wang, X. Wang, H. Gu, B. Chen, Z. Zhang, Z. Ni, H. Jiao, W. Xu, Z. Shi, Y. Yan and J. Huang, *Science*, 2023, **380**, 823–829.

2 H. Wei, Y. Fang, P. Mulligan, W. Chuirazzi, H.-H. Fang, C. Wang, B. R. Ecker, Y. Gao, M. A. Loi, L. Cao and J. Huang, *Nat. Photonics*, 2016, **10**, 333–339.

3 L. Kong, Y. Sun, B. Zhao, K. Ji, J. Feng, J. Dong, Y. Wang, Z. Liu, S. Maqbool, Y. Li, Y. Yang, L. Dai, W. Lee, C. Cho, S. D. Stranks, R. H. Friend, N. Wang, N. C. Greenham and X. Yang, *Nature*, 2024, **631**, 73–79.

4 M. A. Haque, S. Kee, D. R. Villalva, W. L. Ong and D. Baran, *Adv. Sci.*, 2020, **7**, 1903389.

5 X. Zhu, Y. Lin, J. San Martin, Y. Sun, D. Zhu and Y. Yan, *Nat. Commun.*, 2019, **10**, 2843.

6 H. Lu, Z. V. Vardeny and M. C. Beard, *Nat. Rev. Chem.*, 2022, **6**, 470–485.

7 Y. Dong, M. P. Hautzinger, M. A. Haque and M. C. Beard, *Annu. Rev. Phys. Chem.*, 2025, **76**, DOI: 10.1146/annurev-physchem-082423-032933.

8 C. Chen, L. Gao, W. Gao, C. Ge, X. Du, Z. Li, Y. Yang, G. Niu and J. Tang, *Nat. Commun.*, 2019, **10**, 1927.

9 Y.-H. Kim, Y. Zhai, H. Lu, X. Pan, C. Xiao, E. A. Gaulding, S. P. Harvey, J. J. Berry, Z. V. Vardeny, J. M. Luther and M. C. Beard, *Science*, 2021, **371**, 1129–1133.

10 K. Kim, E. Vetter, L. Yan, C. Yang, Z. Wang, R. Sun, Y. Yang, A. H. Comstock, X. Li, J. Zhou, L. Zhang, W. You, D. Sun and J. Liu, *Nat. Mater.*, 2023, **22**, 322–328.

11 H. Lu, J. Wang, C. Xiao, X. Pan, X. Chen, R. Brunecky, J. J. Berry, K. Zhu, M. C. Beard and Z. V. Vardeny, *Sci. Adv.*, 2019, **5**, eaay0571.

12 J. Xu, K. Li, U. N. Huynh, M. Fadel, J. Huang, R. Sundararaman, V. Vardeny and Y. Ping, *Nat. Commun.*, 2024, **15**, 188.

13 A. Privitera, M. Righetto, F. Cacialli and M. K. Riede, *Adv. Opt. Mater.*, 2021, **9**, 2100215.

14 M. Kepenekian and J. Even, *J. Phys. Chem. Lett.*, 2017, **8**, 3362–3370.

15 D. Niesner, M. Wilhelm, I. Levchuk, A. Osvet, S. Shrestha, M. Batentschuk, C. Brabec and T. Fauster, *Phys. Rev. Lett.*, 2016, **117**, 126401.

16 P. Odenthal, W. Talmadge, N. Gundlach, R. Wang, C. Zhang, D. Sun, Z.-G. Yu, Z. Valy Vardeny and Y. S. Li, *Nat. Phys.*, 2017, **13**, 894–899.

17 Y. Zhai, S. Baniya, C. Zhang, J. Li, P. Haney, C.-X. Sheng, E. Ehrenfreund and Z. V. Vardeny, *Sci. Adv.*, 2017, **3**, e1700704.

18 X. Chen, H. Lu, Z. Li, Y. Zhai, P. F. Ndione, J. J. Berry, K. Zhu, Y. Yang and M. C. Beard, *ACS Energy Lett.*, 2018, **3**, 2273–2279.

19 N. Maity, R. Kashikar, S. Lisenkov and I. Ponomareva, *Phys. Rev. Mater.*, 2024, **8**, L091402.

20 T. Etienne, E. Mosconi and F. De Angelis, *J. Phys. Chem. Lett.*, 2016, **7**, 1638–1645.

21 M. A. Pérez-Osorio, R. L. Milot, M. R. Filip, J. B. Patel, L. M. Herz, M. B. Johnston and F. Giustino, *J. Phys. Chem. C*, 2015, **119**, 25703–25718.

22 M. Kepenekian, R. Robles, C. Katan, D. Sapori, L. Pedesseau and J. Even, *ACS Nano*, 2015, **9**, 11557–11567.

23 G. Chen, X. Liu, J. An, S. Wang, X. Zhao, Z. Gu, C. Yuan, X. Xu, J. Bao, H. S. Hu, J. Li and X. Wang, *Nat. Chem.*, 2023, **15**, 1581–1590.

24 J. Ahn, E. Lee, J. Tan, W. Yang, B. Kim and J. Moon, *Mater. Horiz.*, 2017, **4**, 851–856.

25 J. Hao, H. Lu, L. Mao, X. Chen, M. C. Beard and J. L. Blackburn, *ACS Nano*, 2021, **15**, 7608–7617.

26 Y.-H. Kim, Y. Zhai, E. A. Gaulding, S. N. Habisreutinger, T. Moot, B. A. Rosales, H. Lu, A. Hazarika, R. Brunecky, L. M. Wheeler, J. J. Berry, M. C. Beard and J. M. Luther, *ACS Nano*, 2020, **14**, 8816–8825.

27 Y. H. Kim, R. Song, J. Hao, Y. Zhai, L. Yan, T. Moot, A. F. Palmstrom, R. Brunecky, W. You, J. J. Berry, J. L. Blackburn, M. C. Beard, V. Blum and J. M. Luther, *Adv. Funct. Mater.*, 2022, **32**, 2200454.

28 M. A. Haque, A. Grieder, S. P. Harvey, R. Brunecky, J. Y. Ye, B. Addison, J. Zhang, Y. Dong, Y. Xie, M. P. Hautzinger, H. H. Walpitage, K. Zhu, J. L. Blackburn, Z. V. Vardeny, D. B. Mitzi, J. J. Berry, S. R. Marder, Y. Ping, M. C. Beard and J. M. Luther, *Nat. Chem.*, 2025, **17**, 29–37.

29 G. Long, G. Adamo, J. Tian, M. Klein, H. N. S. Krishnamoorthy, E. Feltri, H. Wang and C. Soci, *Nat. Commun.*, 2022, **13**, 1551.

30 H.-Y. Ye, Y.-Y. Tang, P.-F. Li, W.-Q. Liao, J.-X. Gao, X.-N. Hua, H. Cai, P.-P. Shi, Y.-M. You and R.-G. Xiong, *Science*, 2018, **361**, 151–155.

31 T. Feng, Z. Wang, Z. Zhang, J. Xue and H. Lu, *Nanoscale*, 2021, **13**, 18925–18940.

32 Q. A. Akkerman and L. Manna, *ACS Energy Lett.*, 2020, **5**, 604–610.

33 Y. Zheng, X. Han, P. Cheng, X. Jia, J. Xu and X. H. Bu, *J. Am. Chem. Soc.*, 2022, **144**, 16471–16479.

34 S. McKechnie, J. M. Frost, D. Pashov, P. Azarhoosh, A. Walsh and M. van Schilfgaarde, *Phys. Rev. B*, 2018, **98**, 085108.

35 E. Lafalce, E. Amerling, Z. G. Yu, P. C. Sercel, L. Whittaker-Brooks and Z. V. Vardeny, *Nat. Commun.*, 2022, **13**, 483.

36 G. Dresselhaus, *Phys. Rev.*, 1955, **100**, 580–586.

37 E. I. Rashba, *Sov. Phys. Solid State*, 1960, **2**, 1224–1238.

38 X. Zhang, Q. Liu, J.-W. Luo, A. J. Freeman and A. Zunger, *Nat. Phys.*, 2014, **10**, 387–393.

39 Y. A. Bychkov and E. I. Rashba, *JETP Lett.*, 1984, **39**, 78–81.

40 S. Ghosh, B. Pradhan, A. Bandyopadhyay, I. Skvortsova, Y. Zhang, C. Sternemann, M. Paulus, S. Bals, J. Hofkens, K. J. Karki and A. Materny, *J. Phys. Chem. Lett.*, 2024, **15**, 7970–7978.

41 M. K. Jana, R. Song, Y. Xie, R. Zhao, P. C. Sercel, V. Blum and D. B. Mitzi, *Nat. Commun.*, 2021, **12**, 4982.

42 R. Chakraborty, P. C. Sercel, X. Qin, D. B. Mitzi and V. Blum, *J. Am. Chem. Soc.*, 2024, **146**, 34811–34821.

43 X. Chen, H. Lu, K. Wang, Y. Zhai, V. Lunin, P. C. Sercel and M. C. Beard, *J. Am. Chem. Soc.*, 2021, **143**, 19438–19445.

44 J. Wang, C. Zhang, H. Liu, X. Liu, H. Guo, D. Sun and Z. V. Vardeny, *Adv. Mater.*, 2019, **31**, e1904059.

45 J. Wang, C. Zhang, H. Liu, R. McLaughlin, Y. Zhai, S. R. Vardeny, X. Liu, S. McGill, D. Semenov, H. Guo, R. Tsuchikawa, V. V. Deshpande, D. Sun and Z. V. Vardeny, *Nat. Commun.*, 2019, **10**, 129.

46 M. Sharma and D. P. DiVincenzo, *Proc. Natl. Acad. Sci. U. S. A.*, 2024, **121**, e2404298121.

47 E. Lafalce, R. Bodin, B. W. Larson, J. Hao, M. A. Haque, U. Huynh, J. L. Blackburn and Z. V. Vardeny, *ACS Nano*, 2024, **18**, 18299–18306.

48 S. Liu, M. Kepenekian, S. Bodnar, S. Feldmann, M. W. Heindl, N. Fehn, J. Zerhoch, A. Shcherbakov, A. Pöthig, Y. Li, U. W. Paetzold, A. Kartouzian, I. D. Sharp, C. Katan, J. Even and F. Deschler, *Sci. Adv.*, 2023, **9**, eadh5083.

49 I. Abdelwahab, D. Kumar, T. Bian, H. Zheng, H. Gao, F. Hu, A. McClelland, K. Leng, W. L. Wilson, J. Yin, H. Yang and K. P. Loh, *Science*, 2024, **385**, 311–317.

50 D. Giovanni, H. Ma, J. Chua, M. Gratzel, R. Ramesh, S. Mhaisalkar, N. Mathews and T. C. Sum, *Nano Lett.*, 2015, **15**, 1553–1558.

51 D. Giovanni, W. K. Chong, Y. Y. F. Liu, H. A. Dewi, T. Yin, Y. Lekina, Z. X. Shen, N. Mathews, C. K. Gan and T. C. Sum, *Adv. Sci.*, 2018, **5**, 1800664.

52 W. Liang, Y. Li, D. Xiang, Y. Han, Q. Jiang, W. Zhang and K. Wu, *ACS Energy Lett.*, 2021, **6**, 1670–1676.

53 W. Zhao, R. Su, Y. Huang, J. Wu, C. F. Fong, J. Feng and Q. Xiong, *Nat. Commun.*, 2020, **11**, 5665.

54 M. Zhou, J. S. Sarmiento, C. Fei, X. Zhang and H. Wang, *J. Phys. Chem. Lett.*, 2020, **11**, 1502–1507.

55 R. Wang, S. Hu, X. Yang, X. Yan, H. Li and C. Sheng, *J. Mater. Chem. C*, 2018, **6**, 2989–2995.

56 Y. Li, X. Luo, Y. Liu, X. Lu and K. Wu, *ACS Energy Lett.*, 2020, **5**, 1701–1708.

57 S. Strohmair, A. Dey, Y. Tong, L. Polavarapu, B. J. Bohn and J. Feldmann, *Nano Lett.*, 2020, **20**, 4724–4730.

58 S. A. Bourelle, F. V. A. Camargo, S. Ghosh, T. Neumann, T. W. J. van de Goor, R. Shivanna, T. Winkler, G. Cerullo and F. Deschler, *Nat. Commun.*, 2022, **13**, 3320.

59 B. Göhler, V. Hamelbeck, T. Z. Markus, M. Kettner, G. F. Hanne, Z. Vager, R. Naaman and H. Zacharias, *Science*, 2011, **331**, 894–897.

60 B. P. Bloom, Y. Paltiel, R. Naaman and D. H. Waldeck, *Chem. Rev.*, 2024, **124**, 1950–1991.

61 M. P. Hautzinger, X. Pan, S. C. Hayden, J. Y. Ye, Q. Jiang, M. J. Wilson, A. J. Phillips, Y. Dong, E. K. Raulerson, I. A. Leahy, C. S. Jiang, J. L. Blackburn, J. M. Luther, Y. Lu, K. Jungjohann, Z. V. Vardeny, J. J. Berry, K. Alberi and M. C. Beard, *Nature*, 2024, **631**, 307–312.

62 J. Wang, H. Lu, X. Pan, J. Xu, H. Liu, X. Liu, D. R. Khanal, M. F. Toney, M. C. Beard and Z. V. Vardeny, *ACS Nano*, 2021, **15**, 588–595.

63 A. Ishii and T. Miyasaka, *Sci. Adv.*, 2020, **6**, eabd3274.
64 H. Kim, K. Lee, G. Zan, E. Shin, W. Kim, K. Zhao, G. Jang, J. Moon and C. Park, *ACS Nano*, 2025, **19**, 691–703.
65 H. Li, X. Z. Zhao, H. R. Yang, T. M. Guo, W. Li and R. Feng, *Eur. J. Inorg. Chem.*, 2024, **28**, e202400612.
66 H. Lee, C. U. Lee, J. Yun, C. S. Jeong, W. Jeong, J. Son, Y. S. Park, S. Moon, S. Lee, J. H. Kim and J. Moon, *Nat. Commun.*, 2024, **15**, 4672.
67 L. Han, Q. Wang, Y. Lu, S. Tao, W. Zhu, X. Feng, S. Liang, H. Bai, C. Chen, K. Wang, Z. Yang, X. Fan, C. Song and F. Pan, *ACS Nano*, 2024, **18**, 30616–30625.
68 T. M. Guo, F. F. Gao, Y. J. Gong, Z. G. Li, F. Wei, W. Li and X. H. Bu, *J. Am. Chem. Soc.*, 2023, **145**, 22475–22482.
69 M. Ai, L. Pan, C. Shi, Z. F. Huang, X. Zhang, W. Mi and J. J. Zou, *Nat. Commun.*, 2023, **14**, 4562.
70 S. Dhara, E. J. Mele and R. Agarwal, *Science*, 2015, **349**, 726–729.
71 C. Zhang, D. Sun, C. X. Sheng, Y. X. Zhai, K. Mielczarek, A. Zakhidov and Z. V. Vardeny, *Nat. Phys.*, 2015, **11**, 427–434.
72 R. Pan, X. Tang, X. Wang, Y. Liu, L. Huang, Y. Wang, Z. Wang and X. Zhou, *ACS Appl. Mater. Interfaces*, 2024, **16**, 2964–2971.
73 F. Li, J. Ding, W. Yu, X. Guan, P. Wang, D. Wu and T. Wu, *ACS Appl. Mater. Interfaces*, 2020, **12**, 3205–3213.
74 J. Son, S. Ma, Y. K. Jung, J. Tan, G. Jang, H. Lee, C. U. Lee, J. Lee, S. Moon, W. Jeong, A. Walsh and J. Moon, *Nat. Commun.*, 2023, **14**, 3124.
75 H. Lu, C. Xiao, R. Song, T. Li, A. E. Maughan, A. Levin, R. Brunecky, J. J. Berry, D. B. Mitzi, V. Blum and M. C. Beard, *J. Am. Chem. Soc.*, 2020, **142**, 13030–13040.
76 A. Abherve, N. Mercier, A. Kumar, T. K. Das, J. Even, C. Katan and M. Kepenekian, *Adv. Mater.*, 2023, **35**, e2305784.
77 S. Dan, S. Paramanik and A. J. Pal, *ACS Nano*, 2024, **18**, 35644–35653.
78 M.-G. Kang, I.-K. Hwang, H.-C. Kyung, J. Kang, D. Han, S. Lee, J. Kwon, K.-J. Lee, J. Yeom and B.-G. Park, *APL Mater.*, 2024, **12**, 081118.
79 Z. Chen, C. Wang, J. Xue, J. Chen, L. Mao, H. Liu and H. Lu, *Nano Lett.*, 2024, **24**, 3125–3132.
80 Y. Lin, Y. Shao, J. Dai, T. Li, Y. Liu, X. Dai, X. Xiao, Y. Deng, A. Gruverman, X. C. Zeng and J. Huang, *Nat. Commun.*, 2021, **12**, 7.
81 L. Lanzetta, L. Gregori, L. H. Hernandez, A. Sharma, S. Kern, A. M. Kotowska, A.-H. Emwas, L. Gutiérrez-Arzaluz, D. J. Scurr, M. Piggott, D. Meggiolaro, M. A. Haque, F. De Angelis and D. Baran, *ACS Energy Lett.*, 2023, 2858–2867.
82 M. A. Haque, T. Zhu, R. Tounesi, S. Lee, M. Vafaie, L. Huerta Hernandez, B. Davaasuren, A. Genovese, E. H. Sargent and D. Baran, *ACS Nano*, 2024, **18**, 34089–34095.
83 C. Ye, J. Jiang, S. Zou, W. Mi and Y. Xiao, *J. Am. Chem. Soc.*, 2022, **144**, 9707–9714.
84 J. Yao, Y. Huang, H. Sun, Z. Wang, J. Xue, Z. Huang, S.-C. Dong, X. Chen and H. Lu, *Adv. Mater.*, 2025, **37**, 2413669.
85 F. Zhang, B. Cai, J. Song, B. Han, B. Zhang and H. Zeng, *Adv. Funct. Mater.*, 2020, **30**, 2001732.
86 P. A. Dainone, N. F. Prestes, P. Renucci, A. Bouche, M. Morassi, X. Devaux, M. Lindemann, J. M. George, H. Jaffres, A. Lemaitre, B. Xu, M. Stoffel, T. Chen, L. Lombez, D. Lagarde, G. Cong, T. Ma, P. Pigeat, M. Vergnat, H. Rinnert, X. Marie, X. Han, S. Mangin, J. C. Rojas-Sanchez, J. P. Wang, M. C. Beard, N. C. Gerhardt, I. Zutic and Y. Lu, *Nature*, 2024, **627**, 783–788.